Fusion Engineering and Design 218 (2025) 115186

Contents lists available at ScienceDirect

Fusion Engineering and Design

journal homepage: www.elsevier.com/locate/fusengdes

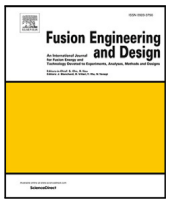

Parametric study of liquid metal flows in conducting rectangular ducts in a strong nonuniform magnetic field

S. Molokov [a,b,*], G. Politis [a], D. Krasnov [b]

[a] UK Atomic Energy Authority (UKAEA), Culham Science Centre, Abingdon, OX14 3DB, United Kingdom
[b] Technische Universität Ilmenau, Postfach 100565, 98684 Ilmenau, Germany

ARTICLE INFO

Keywords:
Liquid metal blankets
Thermonuclear fusion
Magnetohydrodynamics (MHD)
Pressure drop

ABSTRACT

Parametric study of a liquid metal flow in a conducting rectangular duct in a strong, decreasing magnetic field has been performed. Parameters, such as the wall conductance ratio, c, the field gradient, γ, and the aspect ratios of the duct have been varied in the fusion-relevant range. Pressure drop correlations have been obtained for all the cases studied. If the duct is square, the correlation is very similar to the one for a circular duct. Many flow characteristics are similar as well. For a rectangular duct with long sides transverse to the field, three-dimensional (3D) effects are strong. There are very intensive trapped vortices in the nonuniform field region, which have electromagnetic origin. 3D pressure drop increases sharply with the increase of the aspect ratio. For a duct with long walls being parallel to the magnetic field, 3D pressure drop tends to a constant, which depends on c and γ, when the aspect ratio becomes high. The flow velocity across most of the duct's cross-section in the nonuniform field region becomes close to zero, and most of the mass flux is carried by the jets at the walls parallel to the magnetic field.

1. Introduction

In liquid metal blankets for fusion reactors employing either PbLi or Li, most elements involve rectangular ducts of various aspect ratios. As the flow of liquid metals occurs in a high magnetic field of 4-10T, magnetohydrodynamic (MHD) interaction plays a key role in shaping the velocity profiles and in inducing the pressure drop. Because of their importance, various aspects of flows in such ducts have been studied both theoretically and experimentally (see references in [1,2]). The blanket elements involve straight ducts as well as expansions, contractions, manifolds, bends, etc., each producing the so-called *three-dimensional* (3D) effects resulting in significant restructuring of the velocity profiles and in inducing higher, 3D pressure drop compared to straight ducts. Flows in these elements have been studied quite intensively for decades. They will also be investigated experimentally in the future in the CHIMERA facility at UKAEA [3] in an environment as closely emulating a fusion reactor as possible. One of the candidates for such an investigation is the flow in a straight, rectangular, electrically conducting duct in a nonuniform magnetic field. Here we will consider the flow in such a duct in a decreasing magnetic field (Fig. 1) from theoretical point of view.

The flow in a *uniform* magnetic field in rectangular ducts had been investigated theoretically in [4–8] and experimentally in [9–11]. Consider the duct cross-section (Fig. 2). The walls perpendicular to the magnetic field are called the Hartmann walls, while those parallel to the field — the sidewalls. In a high magnetic field, three main distinct regions can be identified: the inviscid core occupying most of the duct cross-section, the Hartmann layers of thickness $\sim (HaB)^{-1}$ located at the Hartmann walls, and the Shercliff layers of thickness $\sim (HaB)^{-1/2}$ at the sidewalls. In the expressions above, Ha is the Hartmann number and $B(x)$ is the local value of the dimensionless magnetic field along the flow normalized by the maximum field inside the magnet, where x is the co-ordinate along the flow.

A typical velocity profile in a duct with conducting walls is shown in Fig. 3. One can observe the distinct core with constant velocity, the Hartmann layers with exponential decay of velocity to zero at the walls, and two Hunt's jets [12] in the Shercliff layers. The jets are very important because they carry part of the mass flux, which is in fine balance with the one carried by the core.

Consider now the *nonuniform* field region. When the magnetic field decreases along the flow, the boundary layers become thicker downstream until they merge with the core and disappear outside of the magnet. For prediction of such flow regimes semi-analytical results can be produced using asymptotic methods for a well-conducting wall. This approach has been widely employed in MHD duct flow analysis by assuming that $c_H \gg Ha^{-1}$ and $c_S \gg Ha^{-1/2}$, where c_H and c_S are

* Corresponding author at: UK Atomic Energy Authority (UKAEA), Culham Science Centre, Abingdon, OX14 3DB, United Kingdom.
E-mail address: sergei.molokov@ukaea.uk (S. Molokov).

https://doi.org/10.1016/j.fusengdes.2025.115186
Received 17 December 2024; Received in revised form 28 March 2025; Accepted 11 May 2025
Available online 4 June 2025

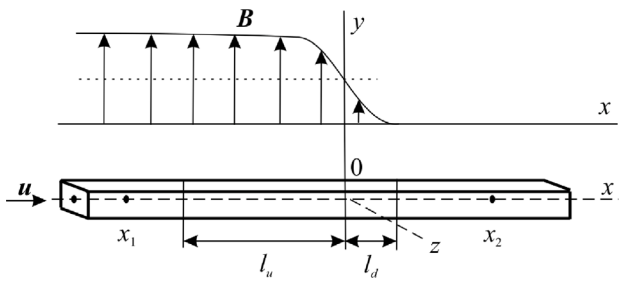

Fig. 1. Liquid metal flow in a rectangular duct in a nonuniform, decreasing magnetic field. Pressure measurements are taken between points $x = x_1$ and $x = x_2$. The development lengths upstream and downstream are l_u and l_d, respectively; (x, y, z) are Cartesian co-ordinates.

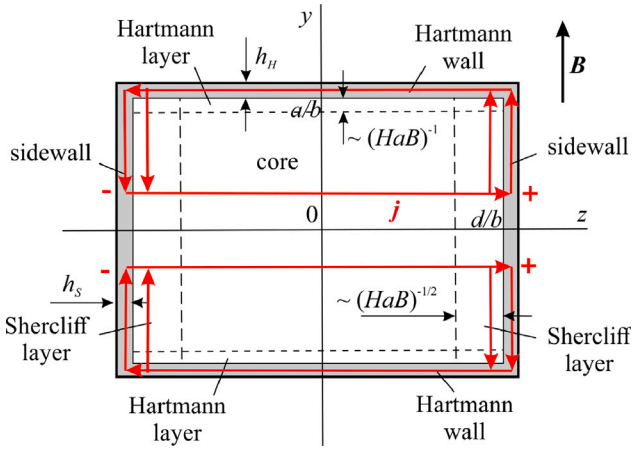

Fig. 2. Flow subregions for $Ha \gg 1$: inviscid core, and viscous Hartmann and Shercliff layers. Induced currents are shown in red. The signs "+ " and "−" indicate induced potential difference between the right and left parts of the duct. Ratios a/b and d/b are the dimensionless height and width of the duct, respectively.

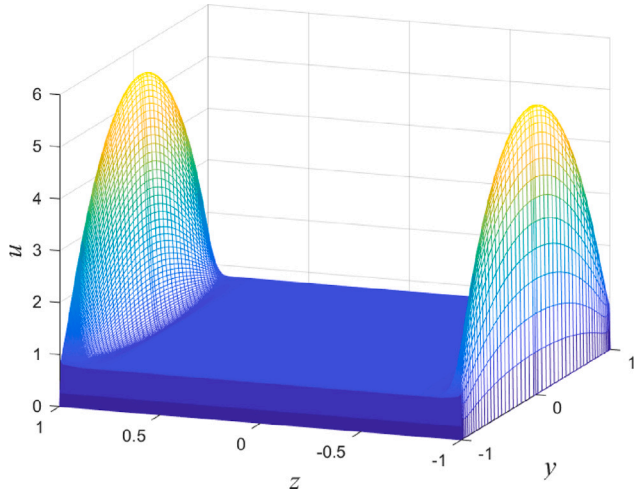

Fig. 3. Axial velocity profile in a fully developed flow in a uniform magnetic field [6] for $Ha = 5,800$ and for the wall conductance ratio $c = 0.0729$.

the wall conductance ratios of the Hartmann- and side-walls, respectively [13]. It results in a system of three two-dimensional equations for the core pressure and the electric potentials of the Hartmann- and the side-walls, which will be presented further in the text. Comparison with the experiment [14] has been very good, and we will use this theory here. In Section 3, we describe the asymptotic model and the CFD one. Then we perform detailed calculations for the experiment [14] (Section 4.1). Finally, parametric studies of the flow are performed, and pressure drop correlations are derived in Section 4.2 for ducts with various aspect ratios.

2. Formulation

Consider an isothermal flow of a viscous, electrically conducting, incompressible fluid along a straight rectangular duct of dimensional height a and width d in the $x-$direction in a strong, transverse magnetic field $\boldsymbol{B} = B(x)\boldsymbol{e}_y$ normalized by B_0, the maximum field inside the magnet. Function $B(x)$ defines the dimensionless variation of the field along the flow, and (x, y, z) are Cartesian co-ordinates. The duct walls are electrically conducting.

The dimensionless equations governing the flow of a liquid metal are [15]:

$$Ha^{-2}\nabla^2\boldsymbol{u} + \boldsymbol{j}\times\boldsymbol{B} = \nabla p + N^{-1}\left\{(\boldsymbol{u}\cdot\nabla)\boldsymbol{u} + \frac{\partial \boldsymbol{u}}{\partial t}\right\}, \tag{1}$$

$$\boldsymbol{j} = -\nabla\phi + \boldsymbol{u}\times\boldsymbol{B}, \tag{2}$$

$$\nabla\cdot\boldsymbol{u} = 0, \tag{3}$$

$$\nabla\cdot\boldsymbol{j} = 0. \tag{4}$$

The length, the time, t, the fluid velocity, $\boldsymbol{u} = (u, v, w)$, the electric current density, $\boldsymbol{j}$, the electric potential, ϕ, and the pressure, p, are normalized by b, b/u_0, u_0, $\sigma u_0 B_0$, $bu_0 B_0$, and $b\sigma u_0 B_0^2$, respectively, where u_0 is the average fluid velocity, σ is its electrical conductivity, and b is the characteristic length, which will be selected later depending on the orientation of the duct to the field (see Section 4.2). The dimensionless parameters are the Hartmann number, $Ha = bB_0(\sigma/\rho\nu)^{1/2}$, and the interaction parameter, $N = b\sigma B_0^2/\rho u_0$. The Reynolds number, Re, can be expressed as follows: $Re = bu_0/\nu = Ha^2/N$. Here ρ and ν are the density and the kinematic viscosity of the fluid, respectively.

The boundary conditions are the no-slip condition for the fluid velocity, and the electrical conditions for a duct with thin conducting walls, namely [15]:

$$\boldsymbol{u} = 0,\ j_y = \mp c_H\left(\frac{\partial^2\phi}{\partial x^2} + \frac{\partial^2\phi}{\partial z^2}\right) \quad \text{at } y = \pm\frac{a}{b}, \tag{5}$$

$$\boldsymbol{u} = 0,\ j_z = \mp c_S\left(\frac{\partial^2\phi}{\partial x^2} + \frac{\partial^2\phi}{\partial y^2}\right) \quad \text{at } z = \pm\frac{d}{b}, \tag{6}$$

where $c_H = \sigma_H h_H/\sigma b$, σ_H, h_H are the wall conductance ratio, the electrical conductivity, and the thickness of the Hartmann walls, respectively, and $c_S = \sigma_S h_S/\sigma b$, σ_S, h_S are corresponding quantities of the sidewalls. The electric boundary conditions of thin walls in Eqs. (5) and (6) are necessary for the asymptotic model only. For calculations with FLUENT the wall is treated as having finite thickness, so these conditions are not used.

3. Asymptotic and numerical models

Two different models to solve Eqs. (1)–(6) have been employed: the asymptotic and the CFD model. They are described below.

3.1. Asymptotic model (AM)

It is assumed that the magnetic field is strong, that inertia is negligible, and that the walls are much better conductors than the adjacent boundary layers, which implies that $Ha \gg 1$, $N \gg Ha^{3/2}$, $c_H \gg Ha^{-1}$, and $c_S \gg Ha^{-1/2}$ [13,15]. The flow is symmetric with respect to axes y and z and is inertialess. Therefore, it is sufficient to calculate the asymptotic solution in the top left quarter only subject to appropriate symmetry conditions.

3.1.1. The core

The flow in the core is governed by three two-dimensional equations below. The derivation involves the same steps as in [13], so the final equations are presented only:

$$\frac{\partial}{\partial x}\left(\beta^2\frac{\partial p_C}{\partial x}\right)+\left(\beta^2+\frac{a^2}{3b^2}\beta'^2\right)\frac{\partial^2 p_C}{\partial z^2}=\beta'\frac{\partial \phi_H}{\partial z}, \tag{7}$$

$$c_H\left[\frac{\partial^2\phi_H}{\partial x^2}+\frac{\partial\phi_H^2}{\partial z^2}\right]=\frac{a}{b}\beta'\frac{\partial p_C}{\partial z}, \tag{8}$$

$$c_S\left[\frac{\partial^2\phi_S}{\partial x^2}+\frac{\partial\phi_S^2}{\partial y^2}\right]=-\beta\left.\frac{\partial p_C}{\partial x}\right|_{z=-d/b}, \tag{9}$$

where $p_C(x,z)$ is the core pressure, $\phi_H(x,z)$ is the electric potential of the top Hartmann wall, $\phi_S(x,y)$ is the one of the left sidewall, $\beta=B^{-1}(x)$, and $\beta'=d\beta/dx$.

The boundary and symmetry conditions are:

$$\frac{\partial p_C}{\partial x}=-k_u B_u^2,\ \frac{\partial\phi_H}{\partial x}=0,\ \frac{\partial\phi_S}{\partial x}=0 \text{ at } x=x_1, \tag{10}$$

$$p_C=0,\ \frac{\partial\phi_H}{\partial x}=0,\ \frac{\partial\phi_S}{\partial x}=0 \text{ at } x=x_2, \tag{11}$$

$$\frac{\partial p_C}{\partial z}=0,\ \phi_H=0 \text{ at } z=0, \tag{12}$$

$$\frac{\partial p_C}{\partial z}=\left(\beta^2+\frac{a^2}{3b^2}\beta'^2\right)^{-1}\times\left\{\beta'\phi_H-\frac{b}{a}\frac{\partial}{\partial x}\left(\beta\int_0^{a/b}\phi_S dy\right)\right\} \text{ at } z=-d/b, \tag{13}$$

$$\frac{\partial\phi_S}{\partial y}=0 \text{ at } y=0, \tag{14}$$

$$\phi_H=\phi_S,\ c_H\frac{\partial\phi_H}{\partial z}=c_S\frac{\partial\phi_S}{\partial y} \text{ at } y=a/b,\ z=-d/b, \tag{15}$$

where

$$k_u=\left|\frac{dp_C}{dx}\right|_u=\left\{1+\frac{a}{bc_H}+\frac{a^2}{3bdc_S}\right\}^{-1} \tag{16}$$

is the absolute value of the pressure gradient in the fully developed flow, and B_u is the dimensionless magnetic field far upstream. Points x_1 and x_2 define the computational domain in the x–direction. Eqs. (15) signify continuity of the electric potential and normal component of wall current at the corner $y=a/b$, $z=-d/b$. The solution for the Hartmann layers can easily be obtained analytically and added to the core.

Once functions p_C, ϕ_H, and ϕ_S are obtained, all other flow quantities for the core can be expressed in terms of these functions. It should be stressed that neither here, nor in a circular conducting pipe [16] the flow is quasi-two-dimensional. Both the core electric potential and all the three components of core velocity in the nonuniform field region are 3D functions depending on all three co-ordinates. For example, the core potential and the longitudinal component of core velocity are:

$$\phi_C(x,y,z)=\phi_H+\frac{1}{2}\beta'\left(y^2-\frac{a^2}{b^2}\right)\frac{\partial p_C}{\partial z}, \tag{17}$$

$$u_C(x,y,z)=-\beta^2\frac{\partial p_C}{\partial x}+\beta\frac{\partial\phi_H}{\partial z}+\frac{1}{2}\beta\beta'\left(y^2-\frac{a^2}{b^2}\right)\frac{\partial^2 p_C}{\partial z^2}. \tag{18}$$

Total flow rate in the duct quarter is:

$$Q=Q_C+Q_{SL}=ad/b^2, \tag{19}$$

where Q_C and Q_{SL} are the flow rates carried by the core and the Shercliff layer, respectively. The flow rate carried by the core is:

$$Q_C(x)=\int_0^{a/b}dy\int_{-d/b}^{0}u_C dz=\frac{a^3}{3b^3}\beta\beta'\left.\frac{\partial p_C}{\partial z}\right|_{z=-d/b}-\frac{a}{b}\beta\left.\phi_H\right|_{z=-d/b}-\frac{a}{b}\beta^2\frac{\partial}{\partial x}\int_{-d/b}^{0}p_C dz. \tag{20}$$

The expression for Q_{SL} will be presented in the next section.

Eqs. (7)–(15) are solved by finite differences on an equidistant, collocated grid by an iterative method [17,18]. Central differences are used throughout. Eqs. (7)–(9) are solved separately from each other with the right-hand sides taken from previous iteration step. Underrelaxation is essential in both the equations and the coupled boundary conditions, especially for low values of the wall conductance ratio. The code is converging fast provided the duct aspect ratio is not very high and wall conductance ratio is not very low.

3.1.2. Shercliff layer at $z=-d/b$

Finding the core velocity is not sufficient because there are high-velocity jets in the Shercliff layers of thickness $\sim [HaB]^{-1/2}$, which carry part of the volume flux. Velocity in these layers is high, $\sim [HaB]^{1/2}$. In order to reconstruct these jets, equations for the Shercliff layer need to be solved once the core quantities are obtained. Consider the layer at $z=-d/b$. In this layer, the boundary-layer corrections to u and v are of order $Ha^{1/2}$, ϕ, j_x, j_y are of order 1, and w, j_z, p are of order $Ha^{-1/2}$. Introducing the stretched variable $\zeta=Ha^{1/2}(z+d/b)$ into Eqs. (1)–(4) and the boundary conditions (5), (6), and neglecting terms of lower order of magnitude compared to those retained, gives:

$$\frac{\partial^2 u_L}{\partial\zeta^2}-j_{z,L}B=\frac{\partial p_L}{\partial x}, \tag{21}$$

$$\frac{\partial^2 v_L}{\partial\zeta^2}=\frac{\partial p_L}{\partial y}, \tag{22}$$

$$j_{x,L}B=\frac{\partial p_L}{\partial\zeta}, \tag{23}$$

$$j_{x,L}=-\frac{\partial\phi_L}{\partial x}-w_L B, \tag{24}$$

$$j_{y,L}=-\frac{\partial\phi_L}{\partial y}, \tag{25}$$

$$\frac{\partial\phi_L}{\partial\zeta}=u_L B, \tag{26}$$

$$\frac{\partial u_L}{\partial x}+\frac{\partial v_L}{\partial y}+\frac{\partial w_L}{\partial\zeta}=0, \tag{27}$$

$$\frac{\partial j_{x,L}}{\partial x}+\frac{\partial j_{y,L}}{\partial y}+\frac{\partial j_{z,L}}{\partial\zeta}=0, \tag{28}$$

where index L denotes the scaled boundary-layer correction to the core variables.

From Eqs. (21)–(28), the following two equations for pressure and electric potential can be derived:

$$\frac{\partial^4 p_L}{\partial\zeta^4}-B^2\frac{\partial^2 p_L}{\partial y^2}=-B'\frac{\partial^3\phi_L}{\partial\zeta^3}, \tag{29}$$

$$\frac{\partial^4\phi_L}{\partial\zeta^4}-B^2\frac{\partial^2\phi_L}{\partial y^2}=B'\frac{\partial p_L}{\partial\zeta}, \tag{30}$$

These equations are coupled in the nonuniform field region only. Outside this region, the equations decouple as in [19].

The boundary and symmetry conditions are:

$$\phi_L=0,\ \frac{\partial p_L}{\partial y}=0 \quad \text{at } y=a/b, \tag{31}$$

$$\frac{\partial\phi_L}{\partial y}=0,\ \frac{\partial p_L}{\partial y}=0 \quad \text{at } y=0, \tag{32}$$

$$\frac{\partial p_L}{\partial \zeta} = -\left.\frac{\partial p_C}{\partial z}\right|_{z=-d/b} + \frac{\partial \phi_S}{\partial x} \quad \text{at } \zeta = 0, \tag{33}$$

$$\frac{\partial^2 p_L}{\partial \zeta^2} = 0 \quad \text{at } \zeta = 0, \tag{34}$$

$$\frac{\partial \phi_L}{\partial \zeta} = -Ha^{-1/2} B\, u_C\big|_{z=-d/b} \quad \text{at } \zeta = 0, \tag{35}$$

$$\phi_L = \phi_S - \phi_C\big|_{z=-d/b} \quad \text{at } \zeta = 0. \tag{36}$$

The term $\sim Ha^{-1/2}$ has been retained in Eq. (35) with the sole purpose of obtaining a continuous solution for the longitudinal velocity valid for both the core and the Shercliff layer [6,20]. Total flow rate carried by the Shercliff layer in the upper left quarter of the duct follows from Eqs. (17) and (26):

$$\begin{aligned} Q_{SL} &= \int_0^{a/b} dy \int_0^{\infty} u_L d\zeta \\ &= -\frac{a^3}{3b^3}\beta\beta' \left.\frac{\partial p_C}{\partial z}\right|_{z=-d/b} + \frac{a}{b}\beta\, \phi_H\big|_{z=-d/b} \\ &\quad - \beta \int_0^{a/b} \phi_S dy. \end{aligned} \tag{37}$$

3.2. CFD model (FLUENT)

The computational methodology employed in this study follows the approach detailed in [16]. ANSYS FLUENT 2023R2 has been utilized, incorporating its finite-volume solver, pressure-based coupled scheme, and inductionless MHD solver to model the interaction between hydrodynamic and Maxwell's equations.

In the axial direction, the computational domain spanned 30 characteristic lengths, evenly divided between the upstream and downstream regions relative to the area of interest. The cross-sectional geometry of the domain has been square, of width equal to 0.0875284 m. Across the various numerical simulations the wall thickness and conductivity have been varied to achieve the desired wall conductance ratio c.

In the axial direction, the computational domain has been discretized with a non-uniform element distribution, ensuring a finer resolution in the region of the fringing magnetic field. This has been achieved by grading the mesh density along the axial axis, concentrating elements in the areas where the magnetic field gradients are most pronounced. To ensure accurate resolution of the Hartmann- and Shercliff-layers, the mesh has been refined near the solid-fluid interfaces by progressively decreasing the element size towards the walls on both sides of the domain. This graded refinement provides sufficient resolution in the regions where the velocity and electromagnetic field gradients are steepest, while maintaining a coarser but adequate element distribution in the bulk fluid region.

In the cross-sectional directions, each Hartmann layer—approximately 7.545×10^{-6} m thick on the top and bottom walls is resolved with 10 elements in the y−direction, and each side layer approximately 5.75×10^{-5} m thick—is resolved with 43 elements in the z−direction; the remaining core region, about 8.6379×10^{-2} m in thickness, is discretized using 75 elements; ensuring a smooth transition from the fine near-wall spacing to the coarser core mesh. The mesh quality is high, with a minimum orthogonality of 0.8 and an average of 0.99998. The final mesh was tested with further refinements to verify that the results do not change appreciably (see Fig. 4).

4. Results

Here we present the results for the tanh −family of fields as in [16]:

$$B(x) = \frac{1}{2}(B_d + B_u) + \frac{1}{2}(B_d - B_u)\tanh(\gamma(x - s)), \tag{38}$$

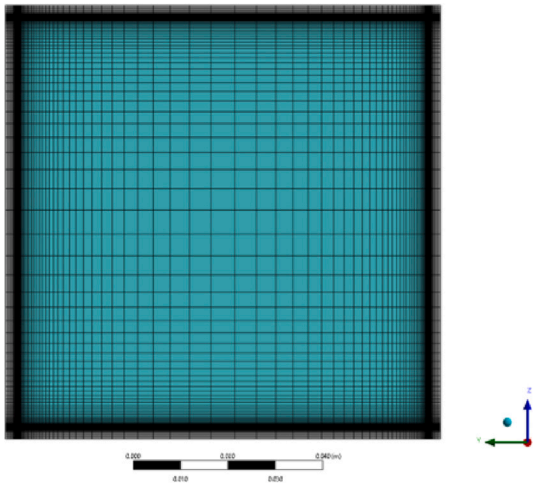

Fig. 4. Mesh in the (y, z)−cross-section of a square duct used in calculations with FLUENT.

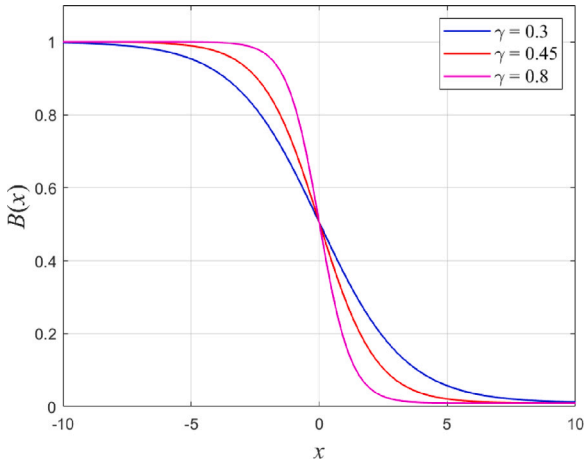

Fig. 5. The magnetic field for the exit duct for three values of the maximum field gradient [16].

where B_d is the value of the uniform magnetic field downstream,

$$\gamma = |dB/dx|_{max} = |dB/dx|_{x=0} \tag{39}$$

is the maximum value of the dimensionless field gradient, and s is the shift of the nonuniform magnetic field along the x-axis. The field for $B_u = 1$, $B_d = 0.01$, $s = 0$, and for three different values of γ is shown in Fig. 5.

4.1. Further results for the experiment by Reed et al. [14]

Detailed calculations for the experiment in [14] have been performed. The parameters of the experiment are:

$$\begin{aligned} c_H &= c_S \equiv c = 0.0729,\ Ha = 5,800,\ N = 126,000, \\ &Re = 267,\ \gamma = 0.359,\ s = 0.765. \end{aligned} \tag{40}$$

The value of the wall conductance ratio is slightly more precise than 0.07 presented in [14] (C.B. Reed, private communication). The duct has square cross-section, so that $b = a = d$, and $a/b = d/b = 1$.

Variation of the negative value of the axial pressure gradient with x is shown in Fig. 6. One can see that both the AM and FLUENT give nearly identical results, which are close to the measurement points. The flow is clearly not fully developed upstream in the experiment, hence the divergence between the curves and the symbols in that region.

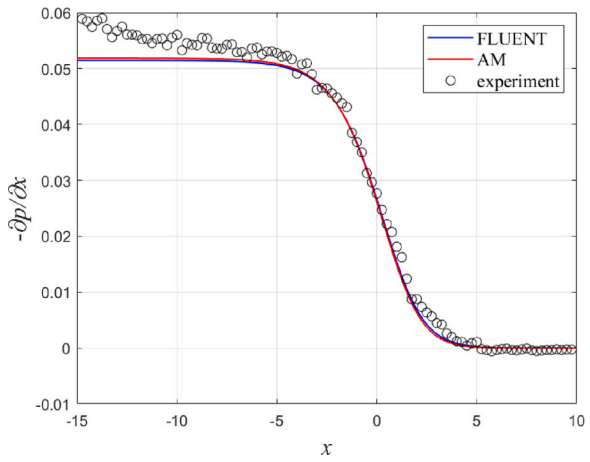

Fig. 6. Negative value of the longitudinal pressure gradient along the x-axis at the sidewall for $y = 0$ and $z = -1$ for the experiment in [14].

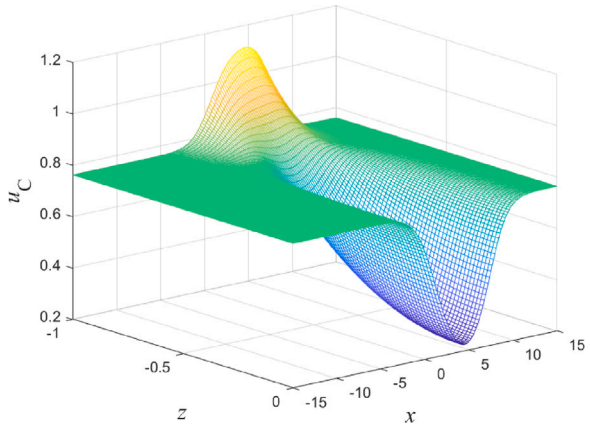

Fig. 7. Development of core velocity profile in the mid-plane $y = 0$ transverse to the magnetic field. (AM).

The development of the core velocity profile at the symmetry plane $y = 0$ is shown in Figs. 7 and 8. Core velocity at the centre of the duct in the nonuniform field region is strongly reduced, but there is no stagnant zone. The fluid flows around the zone with reduced velocity forming thick part of the jets in the core (see the discussion in [16], for example). The picture is incomplete as there are thin parts of the jets closer to the sidewalls in the Shercliff layers, which carry part of the mass flux. This distinguishes these ducts from the circular ones. The full velocity profile at $y = 0$, $x = 0$ for $Ha = 5800$ is shown in Fig. 9. The agreement between AM and FLUENT is very good. The thin jets are clearly visible here. Thick part of the jets is too low for these values of parameters and the position of the cross-section. Further downstream they are more pronounced.

As the flow progresses through the nonuniform field region, another distinguishing feature appears: mass exchange between the core and the Shercliff layers, so that part of the fluid flowing inside these layers is not constant. It first increases as the layers accept part of the fluid from the core, and then decreases by an outflow back (Fig. 10). But as $Q_C > Q_{SL}$ for all values of x, more fluid is carried by the core than by the Shercliff layers everywhere within the flow region.

The electric potentials of the Hartmann- and the side-walls are shown in Fig. 11. These quantities are readily measured in the experiment. It is the fall of the magnitude of the sidewall potential along the flow that drives the 3D currents.

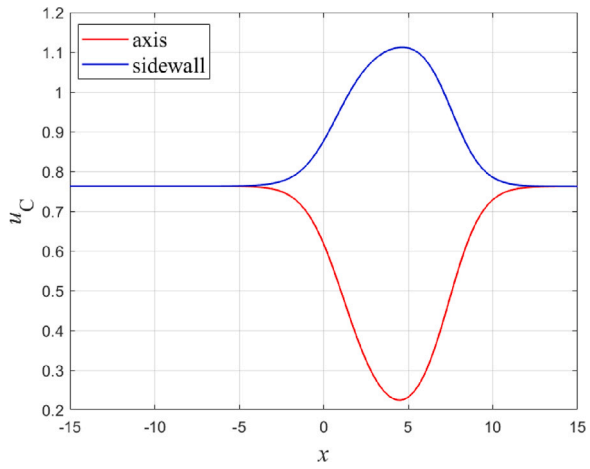

Fig. 8. Development of core velocity along the duct axis at $y = 0$, $z = 0$ (axis) and at $y = 0$, $z = -1$ (sidewall).(AM).

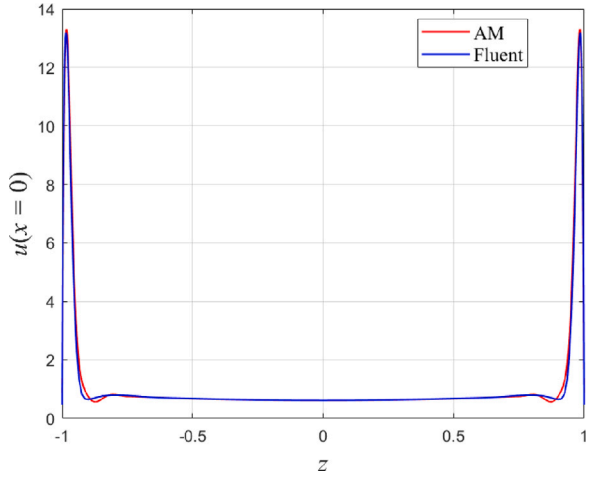

Fig. 9. Full axial velocity profile at $y = 0$, $x = 0$.

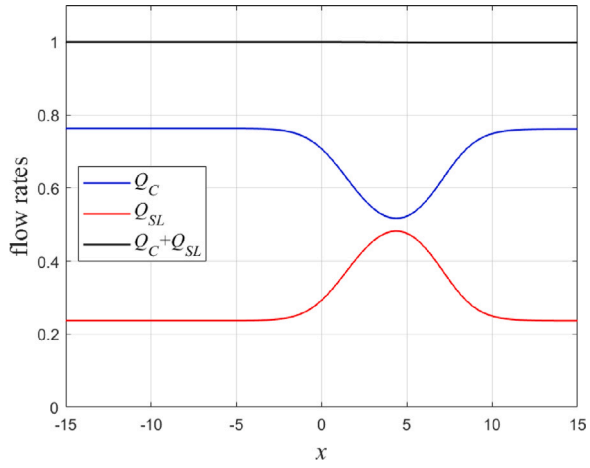

Fig. 10. Development of flow rates carried by the core and the Shercliff layer along the flow in the quarter of the duct. (AM).

The expression for the dimensional pressure drop between two points, x_1 and x_2, encompassing the nonuniform field region is:

$$\triangle p^* = \sigma b u_0 B_0^2 \left[\triangle p_{lfd} + \triangle p_{3D}\right], \tag{41}$$

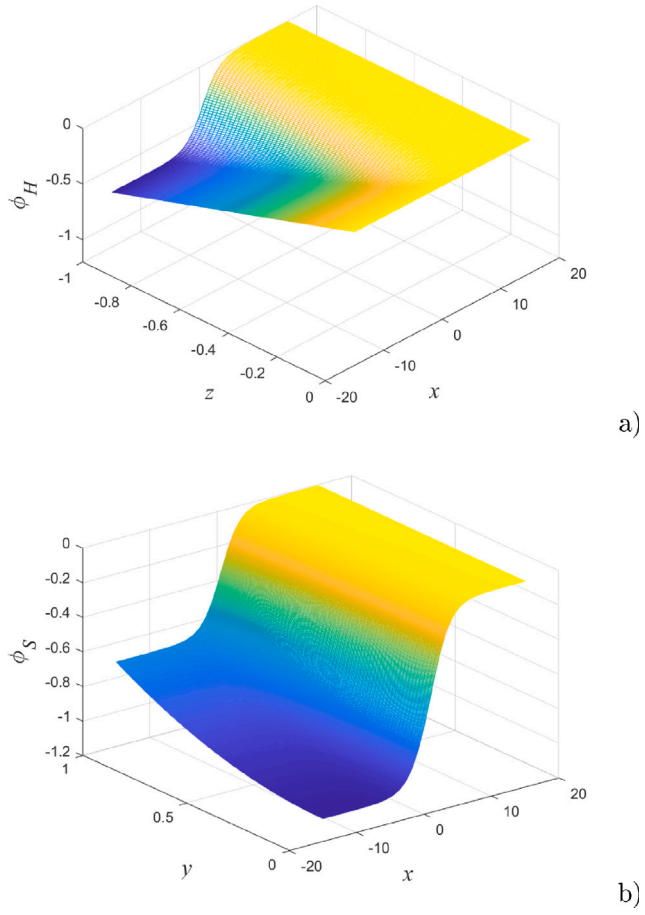

Fig. 11. Electric potentials of the Hartmann wall (a) and the sidewall (b). (AM).

Table 1
Summary of key characteristics of the flow for the experimental setup in [14].

Quantity	Notation	Value
maximum core velocity	u_{max}	1.112
minimum core velocity	u_{min}	0.224
position of minimum	x_{min}	4.500
pressure gradient upstream	$(dp_C/dx)_u$	−0.052
3D pressure drop	$\triangle\, p_{3D}$	0.024
3D length	d_{3D}	0.454
development length upstream	l_u	4.620
development length downstream	l_d	13.140
length of the stagnant zone	l_{st}	0

where

$$\triangle\, p_{lfd} = k_u \int_{x_1}^{x_2} B^2(\xi) d\xi. \tag{42}$$

is the pressure drop in the locally fully developed flow [13], and $\triangle\, p_{3D}$ is an additional, 3D pressure drop due to the 3D currents (Fig. 12). Correlations for $\triangle\, p_{3D}$ for various cases will be obtained below.

Other main 3D flow characteristics are defined as follows. The development length upstream, l_u, is equal to the value $|x|$ when the core velocity at the axis starts deviating from its fully developed value by more than 0.1%. The development length, l_d, is defined in a similar way (Fig. 1). The length of the stagnant zone, l_{st}, is defined as the distance between the two points for which the core velocity along the axis falls below 0.05. The 3D length is defined in a conventional way:

$$d_{3D} = \left| \triangle\, p_{3D} / \left(dp_C/dx\right)_u \right|. \tag{43}$$

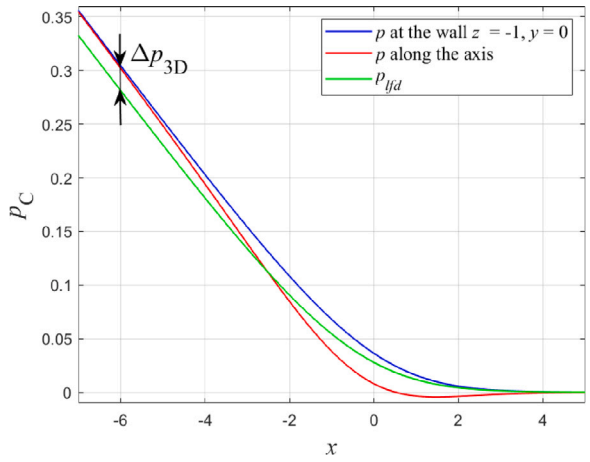

Fig. 12. Distribution of core pressure for Reed's experiment along the duct axis and along $z = -1$ at $y = 0$; pressure in a locally fully developed flow, and the definition of the 3D pressure drop Δp_{3D}.(AM).

It is the length by which the straight duct needs to be extended to account for $\triangle\, p_{3D}$. Key flow characteristics for this experiment are shown in Table 1. As with the circular ducts, the 3D currents have low influence on the pressure drop as evidenced by low value of the 3D length. From the results presented above follows that the 3D effects on the velocity profiles are not very high either. We will see much stronger 3D effects below.

4.2. Variation of parameters and pressure drop correlations

Now we consider variation of key flow characteristics with the parameters for $B_u = 1$, $B_d = 0.01$, and $s = 0$. For the sake of simplicity, we assume that the wall conductance ratios of the Hartmann- and sidewalls are equal: $c_H = c_S = c$. Parameters c and γ have been varied in the range $0.01 \le c \le 0.5$ and $0.3 \le \gamma \le 0.8$ relevant to fusion. Calculations have been performed by the asymptotic model. As Ha^{-1} scales out of the problem for the core flow given by Eqs. (7)–(15), its exact value is irrelevant, but the following relation must be satisfied: $c \gg Ha^{-1/2}$ for each combination of c and Ha.

4.2.1. Square duct

Here $b = a = d$, so that $a/b = d/b = 1$, and

$$k_u = \frac{c}{c + \frac{4}{3}}.$$

Variation of key flow characteristics with the wall conductance ratio is shown in Fig. 13 for three different values of γ. Compared to circular ducts [16], one can see that the results are similar both qualitatively and quantitatively. The more steeply the field varies, the more severe is the deformation of the core velocity profile in the nonuniform field region. The stagnant zone exists for all the values of γ provided the value of c is sufficiently small. For $\gamma = 0.8$, the stagnant zone exists for all values of c. The development length upstream is not too high. It is below the value of 6 for all values of c and γ (Fig. 13d). The 3D pressure drop grows with increasing c (Fig. 13e), but its contribution to the total pressure drop decreases as evidenced by falling 3D length (Fig. 13f). If c was increased further, there would be a maximum of $\triangle\, p_{3D}$, after which it would be decreasing as discussed in [16]. But for a square duct, the value of $c = 0.5$ is evidently too low to reach that stage.

Now we will obtain the correlation for the 3D pressure drop. We adopt the strategy developed in [16]. The 3D length varies nearly

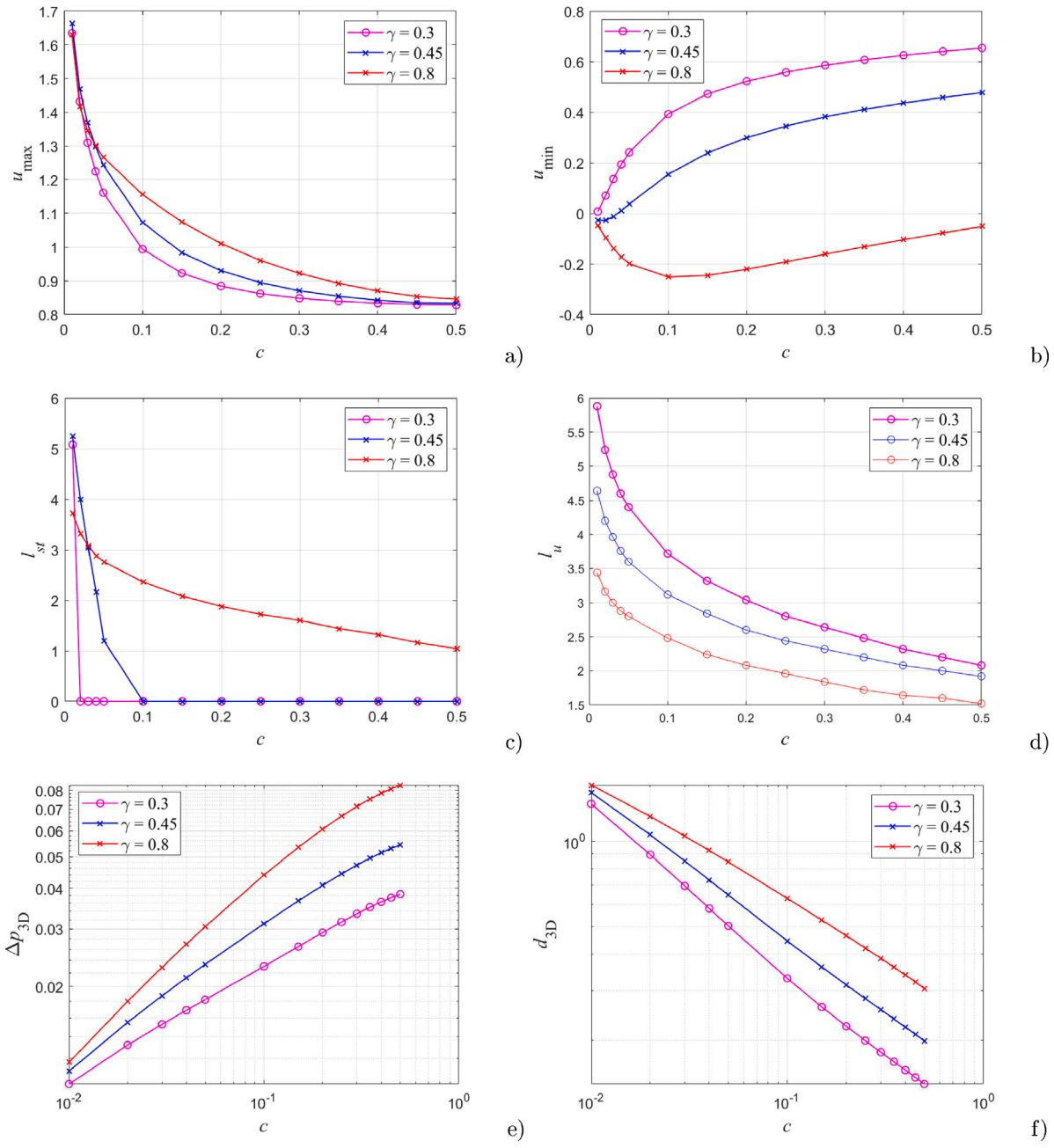

Fig. 13. Maximum (a) and minimum (b) of core velocity at $y = 0$, the stagnant zone length (c), the development length upstream (d), the 3D pressure drop (e) and the 3D length (f) for a square duct as functions of c for three values of the field gradient. (AM).

linearly with c in the log–log plot (Fig. 13f), which suggests a power-law dependence. The following correlation for d_{3D} has been found to fit best:

$$d_{3D} \approx 0.296\gamma^{0.949} c^{(0.317\gamma - 0.662)}. \tag{44}$$

The agreement between the fit and the data points is very good (Fig. 14). Once d_{3D} is found, the correlation for the 3D pressure drop becomes:

$$\triangle\, p_{3D} = d_{3D} \left| \frac{dp_c}{dx} \right|_u \approx \frac{0.296\gamma^{0.949} c^{(0.317\gamma + 0.338)}}{c + \frac{4}{3}}, \tag{45}$$

and the total, dimensional pressure drop between points x_1 and x_2 is calculated from Eqs. (41), (42), and (45). Eq. (45) is very similar to the corresponding result for the circular conducting pipe [16] both in structure and in the values of coefficients.

We will also need the values of the electric potentials of the walls for future reference. They are shown in Fig. 15.

4.2.2. Rectangular duct with long walls transverse to the field for $\gamma = 0.45$

Now we vary the width of the duct, d, while keeping the height, a, constant. Then

$$b = a,\ c = \frac{\sigma_w h_w}{\sigma a},\ k_u = \frac{c}{1 + c + (3D)^{-1}}, \tag{46}$$

where $D = d/a$ is the aspect ratio. This expression for k_u has been derived first by Miyazaki et al. [21]. Note that $k_u \to c/(1+c)$ as $D \to \infty$, i.e. it increases and tends to the pressure gradient in the Hartmann- and circular-duct- flows [15]. Total flow rate in the duct quarter is equal to D.

Core velocity profiles at the centre of the nonuniform field region, $x = 0$, $y = 0$ are shown in Fig. 16 for various values of the aspect ratio.

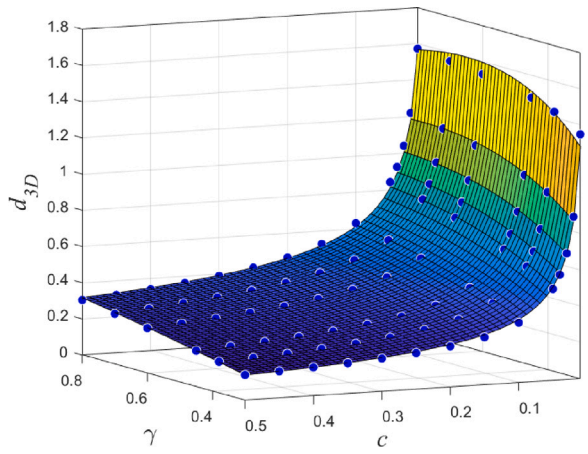

Fig. 14. Comparison between calculated values of the 3D length (blue circles) and the fit (44) (surface) for a square duct.(AM).

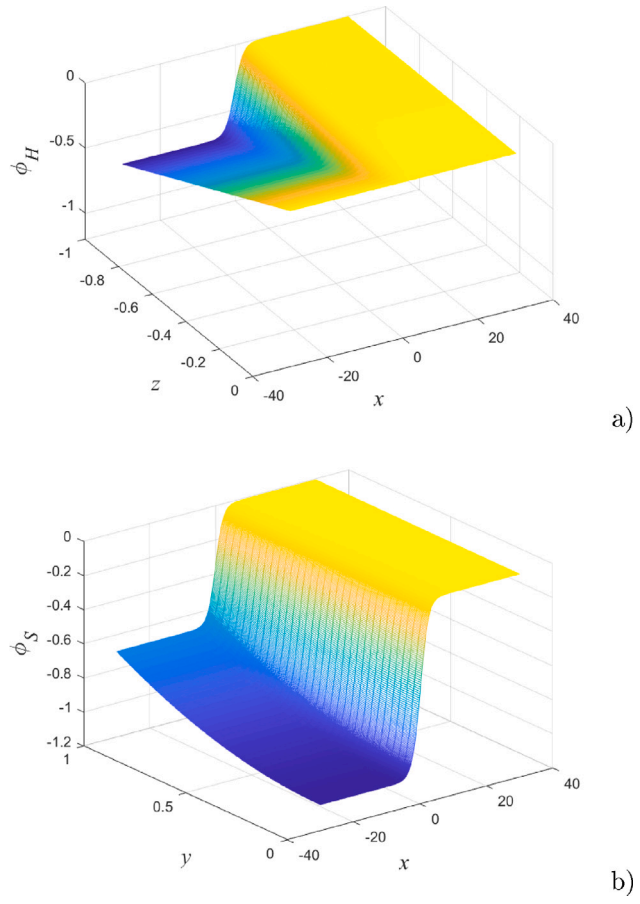

Fig. 15. Electric potentials of the Hartmann wall (a) and the sidewall (b) for a square duct. Here $c = 0.1$, $\gamma = 0.45$. (AM).

One can see that, for $D > 1$, the velocity in the central half of the ducts is nearly constant. The rest of the duct cross-section is occupied by thick parts of the jets (a quarter of the duct width each). Thin parts located within the Shercliff layers not shown also carry significant share of the mass flux especially in the nonuniform field region. The development of the proportion of the flow rate carried by them is shown in Fig. 17a. Far upstream, at $x = -15$, the layers' importance decreases with the increase of D as more and more fluid is carried by the wide, flat core (Fig. 17b). But as the flow progresses into the nonuniform region,

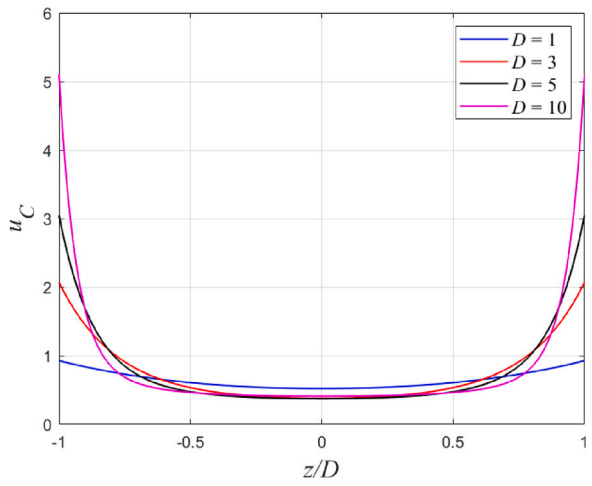

Fig. 16. Core velocity profiles at the centre of the nonuniform field region $x = 0$, $y = 0$ for $c = 0.1$, $\gamma = 0.45$ and for several values of D. (AM).

the 3D currents appear, and the picture reverses. The currents become stronger as transverse potential difference between the sidewalls grows (Fig. 18), and more and more fluid is driven from the core into the Shercliff layers. For $D = 10$, Q_{SL}/D becomes higher than one, i.e. the layer carries more than the total flow rate over a certain distance. At the same time, Q_C/D falls below zero by the same amount. Together this implies very strong recirculation of the fluid in the nonuniform field region involving both the core and the layers.

Key 3D flow characteristics for different values of c are shown in Fig. 19. It is seen that all of them grow sharply with increasing aspect ratio. The deformation of the core velocity profile can be deduced from Figs. 19a,b. The maximum value of the core velocity calculated over the whole flow domain reaches the value above 30 for $c = 0.05$. It should be reminded that this part of the velocity profile is independent of the Hartmann number. Furthermore, three observations can be made. Firstly, there is practically no difference in values of u_{max} for low values of c, which implies that it possibly reaches some kind of limit as c decreases. However, there is a considerable difference in u_{min}. Secondly, the minimum of the core velocity is reached for an intermediate value of $c = 0.1$, not for the lowest value of c. Thirdly, the intensity of the recirculating flow increases sharply as D increases. For $c = 0.1$ and $D = 10$, the reverse flow involves velocities of -3.

The length of the stagnant zone may reach almost 13 values of the characteristic length (Fig. 19c). Also, for high D, there is almost no difference between the results for $c = 0.05$ and $c = 0.1$. The same is true for the development length upstream, which may reach the value of 23, i.e. the 3D effects spread well upstream of the nonuniform field region.

The graphs of $\triangle\ p_{3D}$ and d_{3D} are shown in Fig. 19e and Fig. 19f, respectively. The 3D pressure drop grows by an order of magnitude as D increases to 10. Its contribution to the total pressure drop also grows sharply. The 3D length can reach the value of 12, which means that the 3D pressure drop gains its importance significantly. Finding a single, satisfactory correlation for $\triangle\ p_{3D}$ with three independent parameters, c, γ, and D proved to be difficult. Therefore, it has been obtained for $\gamma = 0.45$, which is typical for two-pole magnets. The result for d_{3D} is:

$$d_{3D} \approx 0.186 c^{-0.491} D^{-0.232c+1.178}.$$

Then,

$$\triangle\ p_{3D} = k_u d_{3D} \approx 0.186 \frac{c^{0.509} D^{-0.232c+1.178}}{1 + c + (3D)^{-1}}. \quad (47)$$

Comparison of values obtained from this correlation with the data points is shown in Fig. 20. The agreement with the data is vey good.

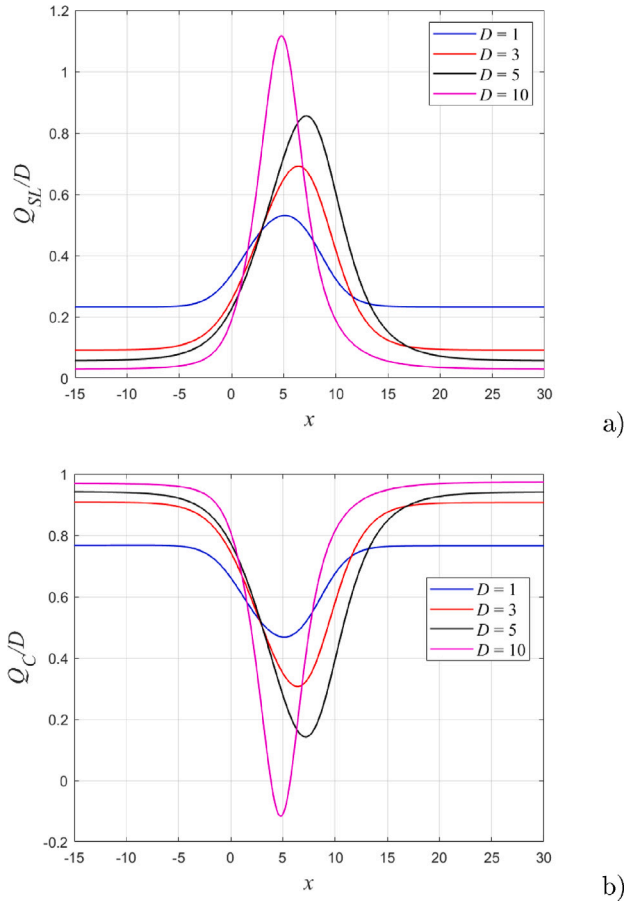

Fig. 17. Development of flow rate fractions carried by the Shercliff layer (a) and the core (b) for $c = 0.1$, $\gamma = 0.45$ and for several values of D. (AM).

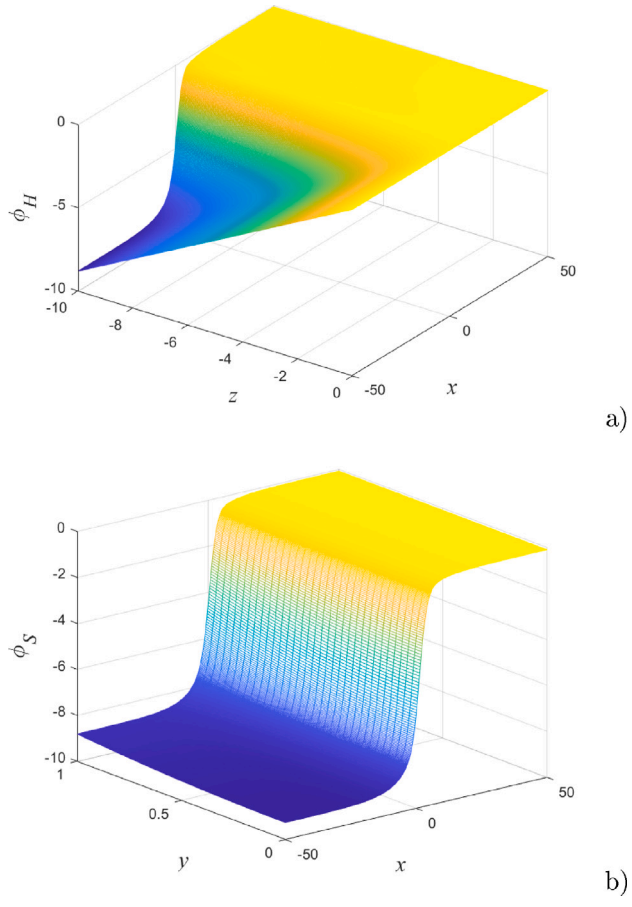

Fig. 18. Electric potentials of the Hartmann wall (a) and the sidewall (b) for $c = 0.1$, $\gamma = 0.45$, $D = 10$. (AM).

4.2.3. Rectangular ducts with long walls parallel to the field for $\gamma = 0.45$

Now we vary the height of the duct, a, while keeping the width, d, constant. Then it is logical to take d as the characteristic length [13], so that

$$b = d,\ c = \frac{\sigma_w h_w}{\sigma d},\ k_u = \frac{c}{c + A + \frac{1}{3}A^2}, \tag{48}$$

where $A = a/d$ is the aspect ratio. The total flow rate in the duct quarter is equal to A. Upstream pressure gradient, k_u, tends to zero as A increases, which implies a well-known fact that it becomes easier to pump the fluid through a slotted duct whose cross-section is aligned with the field. If the field was uniform and the Hartmann walls were removed to infinity, the magnetic field would be parallel to the only two remaining sidewalls, and there would be no MHD interaction, hence no MHD pressure drop. The result would be pure plane Poisseuille flow. However, the transformation to this state as A increases is very complex, and involves merging of the two Shercliff layers, a formation of the wake-like structures, etc. This is beyond the scope of the current investigation.

As the distance between the sidewalls remains constant, the sidewall potential does not increase in magnitude (compare Fig. 21b for $A = 10$ with Fig. 15b for $A = 1$), and thus the potential drop along the flow remains of similar magnitude. Therefore, the 3D currents remain similar in magnitude too, and the 3D pressure drop tends to a constant, which depends on both c and γ. Although this constant is small, its contribution to the total pressure drop increases (Fig. 22f) because $k_u \to 0$ as A increases. The correlations for $\triangle p_{3D}$ and d_{3D} for $\gamma = 0.45$ are:

$$d_{3D} \approx 0.155 c^{-0.084} A^{0.061c+1.555}, \tag{49}$$

$$\triangle p_{3D} = k_u d_{3D} \approx 0.155 \frac{c^{0.916} A^{0.061c+1.555}}{c + A + \frac{1}{3}A^2}. \tag{50}$$

Comparison between the correlation for d_{3D} and the data points, shown in Fig. 23, is quite satisfactory, especially for higher values of c and A.

Consider now the effect of increasing A on the velocity profiles. Fig. 24 shows core velocity at the centre of the nonuniform field region $x = 0$, $y = 0$. The core velocity decreases with increasing A and becomes slightly negative for $A = 10$. The minimum of the core velocity in the whole flow region is negative for all values of c (Fig. 22b). Consider portions of the flow rates carried by the core and the Shercliff layer (Fig. 25). Far upstream in the uniform field region [13],

$$\frac{Q_{SL}}{A} = \left(1 + \frac{3}{A} + \frac{3c}{A^2}\right)^{-1}. \tag{51}$$

Therefore, nearly all the fluid is carried by the layer for high values of A. 3D currents strengthen this effect in the nonuniform region. For $A = 10$ and $c = 0.1$, the layer carries more than the total volume flux over some distance (Fig. 25a). This is accompanied by negative volume flux carried by the core over the same length of the duct. As with high D, we see two trapped vortices at the centre, which can be quite long (Fig. 22c). Interestingly, the maximum of the core velocity becomes nearly independent of the value of c for $A \geq 2$ (Fig. 22a).

To conclude this section two observations can be made: (i) the 3D effects are weaker for high values of A than for high values of D, (ii) for high values of A most of the flow is carried by Shercliff layers throughout the whole domain.

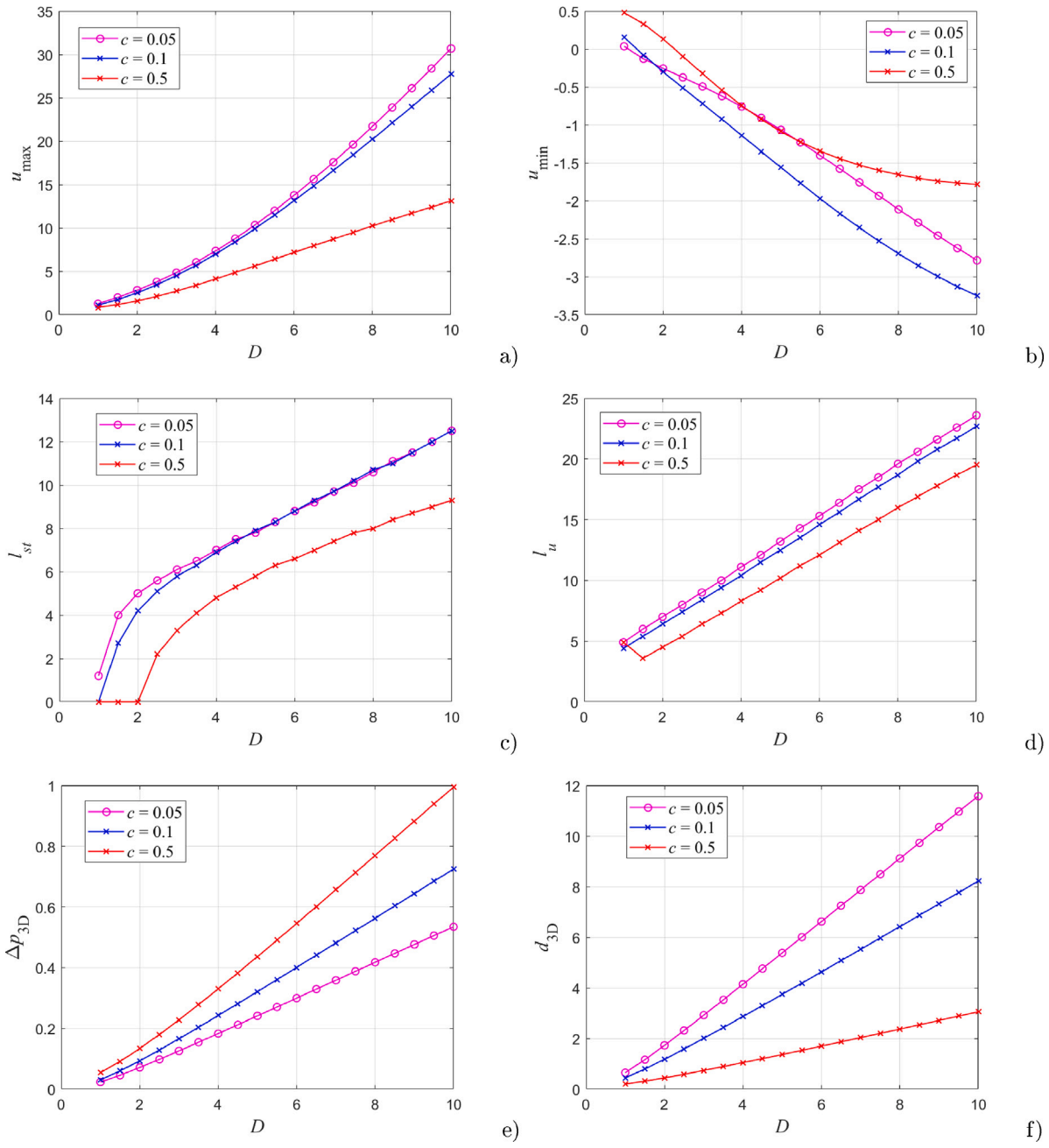

Fig. 19. Maximum (a) and minimum (b) of core velocity at $y = 0$; the stagnant zone length (c), the development length upstream (d), the 3D pressure drop (e) and the 3D length (f) as functions of D for three values of c. Here $\gamma = 0.45$.(AM).

5. Discussion and conclusions

Liquid metal flow in a rectangular duct in a strong, nonuniform magnetic field has been studied for a wide range of parameters relevant to fusion, such as the wall conductance ratio, c, the value of the field gradient, γ, and the aspect ratios, A or D.

The velocity profile upstream of the nonuniform field region involves a flat core occupying most of the duct cross-section and high-velocity jets of thickness $\sim (HaB)^{-1/2}$ at the sidewalls. Both the core and the jets carry parts of the mass flux as the velocity of the thin jets is high, $\sim (HaB)^{1/2}$. As the fluid passes through the nonuniform field region further downstream, it has to flow around the zone with reduced velocity or even a recirculating flow located in the core. Fine flow balance between the core and the thin jets changes during this process. Two effects occur. First of all, thick parts of the jets appear on the core side, and thus the magnitude of velocity of these parts is independent of the Hartmann number. Secondly, the mass flow balance between the core and the Shercliff layers changes by the inflow of part of the fluid into the layers and then an outflow at the end of the nonuniform field region. This effect becomes stronger if c decreases, or if the aspect ratios or γ increase.

The most interesting effects occur if the width of the duct is high (aspect ratio D), or if the height of the duct is high (aspect ratio A). If D is high, the potential difference between the sidewalls grows. Therefore, the drop in magnitude of the a sidewall potential along the duct grows too. As it is this drop in potential that drives the 3D currents, they become stronger implying stronger 3D effects. All the 3D flow characteristic properties of the flow grow: the deformation of the core velocity profile, the length of the stagnant zone, the development length, the 3D length, and the 3D pressure drop. For $D = 10$, the

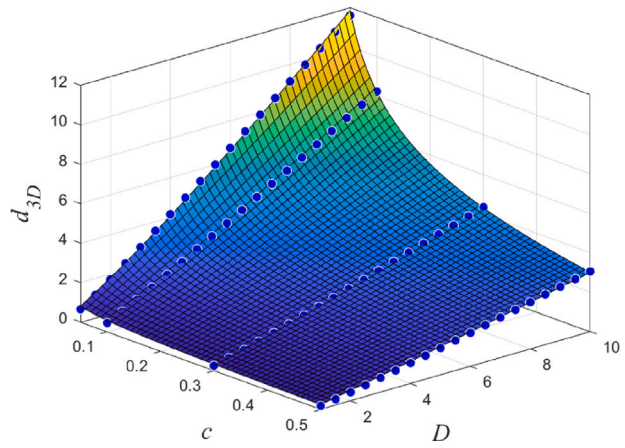

Fig. 20. Comparison between calculated values of the 3D length (blue circles) and the fit (44) (surface) for a duct with long walls transverse to the field.(AM).

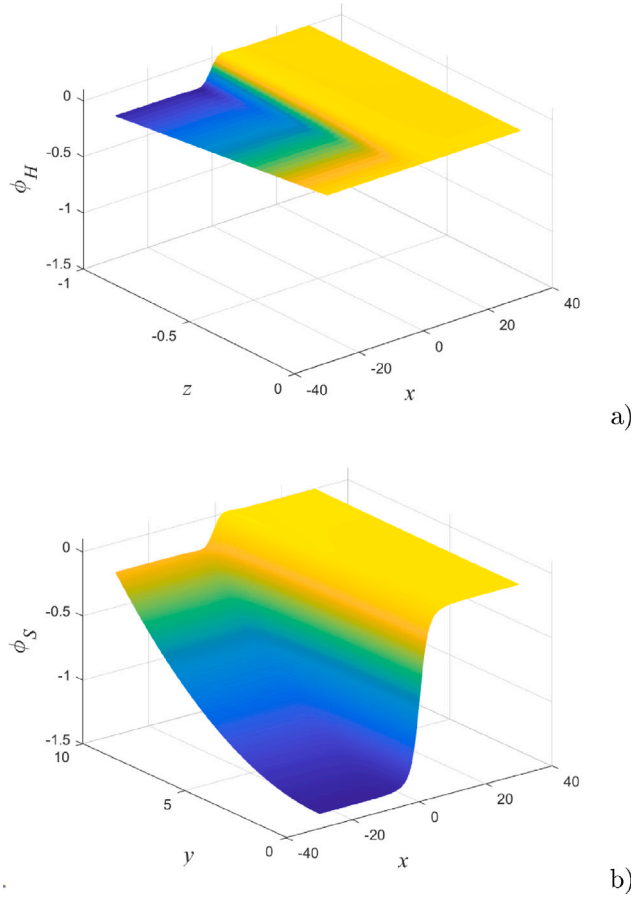

Fig. 21. Electric potentials of the Hartmann wall (a) and the sidewall (b) for $c = 0.1$, $\gamma = 0.45$, $A = 10$. (AM).

Shercliff layers carry more than the total mass flux in the nonuniform field region. At the same time, the fluid velocity in the core flows in the reverse direction at up to 3 values of the average velocity of the fluid. Such an extreme flow is bound to become unstable for relatively low values of N. This may involve shedding of large-scale vortices downstream, which is an interesting topic for a future investigation.

If the distance between the sidewals is fixed and A increases, the potential difference between the sidewalls does not increase, and the 3D pressure drop tends to a constant, which depends on c and γ. But the stagnant zone length, the development length and the 3D length all increase. For $A = 10$, the flow in the core is reversed throughout the whole nonuniform field region and beyond. At the same time, the Shercliff layers carry more than the total mass flux over this distance.

Several observations can be made at the end. First of all, some flow features, such as the development of the jets or mass exchange between the core and the Shercliff layers continues or even reaches its peak at or after the end of the nonuniform field region. For $\gamma = 0.45$ it happens for $x > 5$ (Fig. 5). This is acceptable for the value of the uniform field downstream of $B_d = 0.01$, but the pattern may be different for $B_d = 0$. This issue is beyond the limit of the current asymptotic model.

Secondly, the assumption $c \gg Ha^{-1/2}$ may be quite restrictive. Figs. 6 and 26 illustrate this point. The value of the Hartmann number in these calculations is $Ha = 5800$ ($Ha^{-1/2} = 0.0131$). For $c = 0.5$ and for $c = 0.0729$ the accuracy of the asymptotic model is very good, but for $c = 0.02$ it is inadequate because the condition $c \gg Ha^{-1/2}$ is violated. Therefore, caution must be exercised when applying the correlations for very small values of c and moderately high values of Ha. The work on relaxing this assumption is ongoing.

Next, the magnetic field here is nonuniform, but it contains only one component in the y−direction. Strictly speaking, such a field is not *curl*−free, so that the second, smaller component exists in the x−direction. The effect of the second component on the flow has been studied for various duct geometries [22–26] and specifically for this duct geometry in [27]. Taking this component into account leads to somewhat better approximation to the transverse pressure difference (by up to 15%) to the corresponding experimental values in [14]. Therefore, the values of the core velocity may be affected by a similar amount. But the longitudinal pressure gradient and thus the pressure drop are not affected (see comparison in [14] for a field with one component only and in Fig. 6 here).

Finally, high-velocity jets are known to be prone to linear instability [28–30], finite-amplitude structures [7,31,32], or turbulence [9,10] if certain conditions are not met, but this is out of scope of this investigation.

CRediT authorship contribution statement

S. Molokov: Writing – review & editing, Writing – original draft, Software, Methodology, Investigation. **G. Politis:** Writing – review & editing, Writing – original draft, Investigation. **D. Krasnov:** Investigation.

Declaration of competing interest

The authors declare that they have no known competing financial interests or personal relationships that could have appeared to influence the work reported in this paper.

Acknowledgements

This work has been carried out within the framework of the EUROfusion Consortium, funded by the European Union via the Euratom Research and Training Programme (Grant Agreement No 101052200 — EUROfusion) and from the EPSRC, United Kingdom [grant number EP/W006839/1]. Views and opinions expressed are however those of the author(s) only and do not necessarily reflect those of the European Union or the European Commission. Neither the European Union nor the European Commission can be held responsible for them. To obtain further information on the data and models underlying this paper please contact PublicationsManager@ukaea.uk.

Data availability

To obtain further information on the data and models underlying this work please contact PublicationsManager@ukaea.uk.

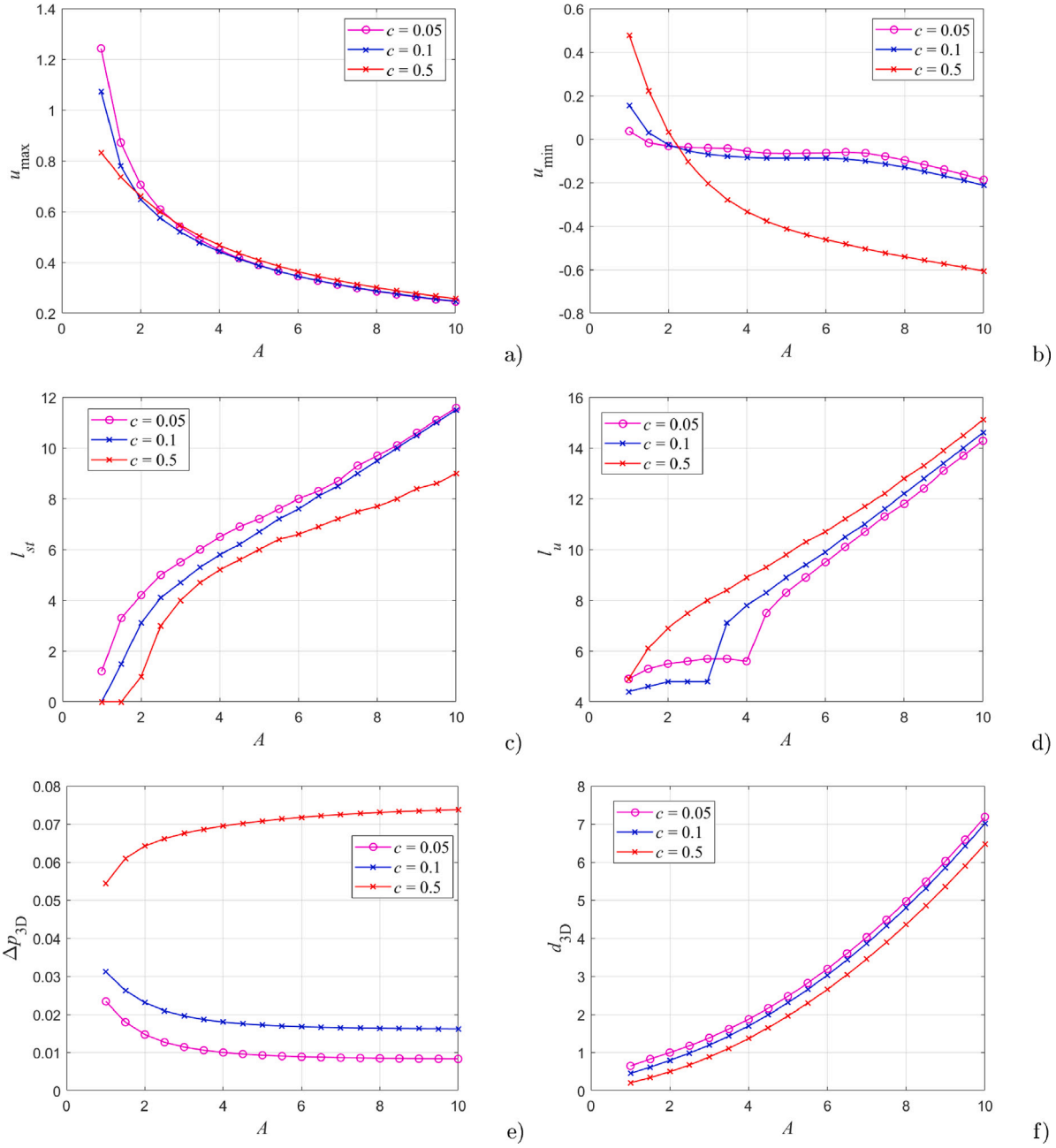

Fig. 22. Maximum (a) and minimum (b) of core velocity at $y = 0$; stagnant zone length (c), development length upstream (d), the 3D pressure drop (e) and the 3D length (f) as functions of A for three values of c. Here $\gamma = 0.45$.(AM).

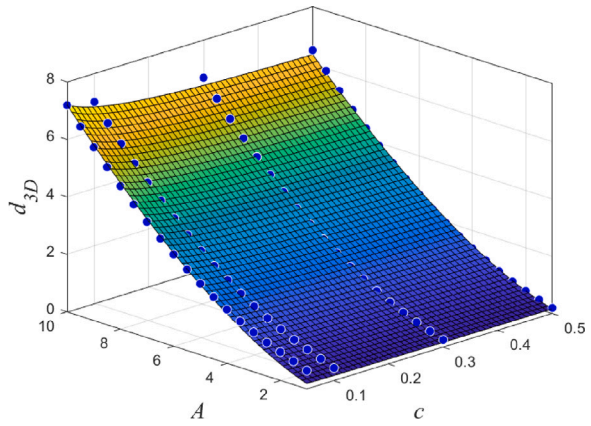

Fig. 23. Comparison between calculated values of the 3D length (blue circles) and the fit (44) (surface) for a duct with long walls being parallel to the field.(AM).

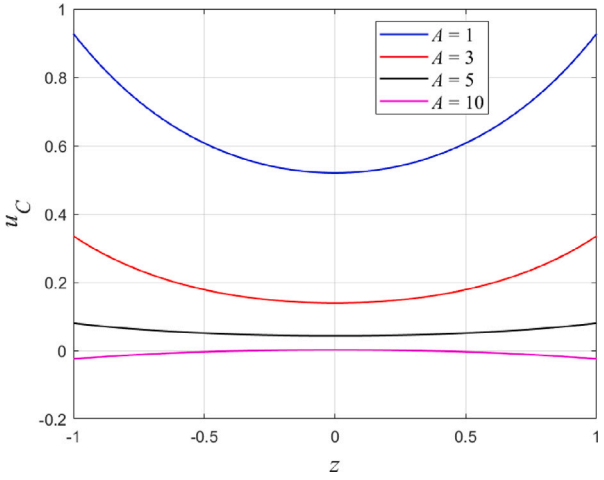

Fig. 24. Core velocity profiles at the centre of the nonuniform field region $x = 0$, $y = 0$ for $c = 0.1$, $\gamma = 0.45$ and for several values of A. (AM).

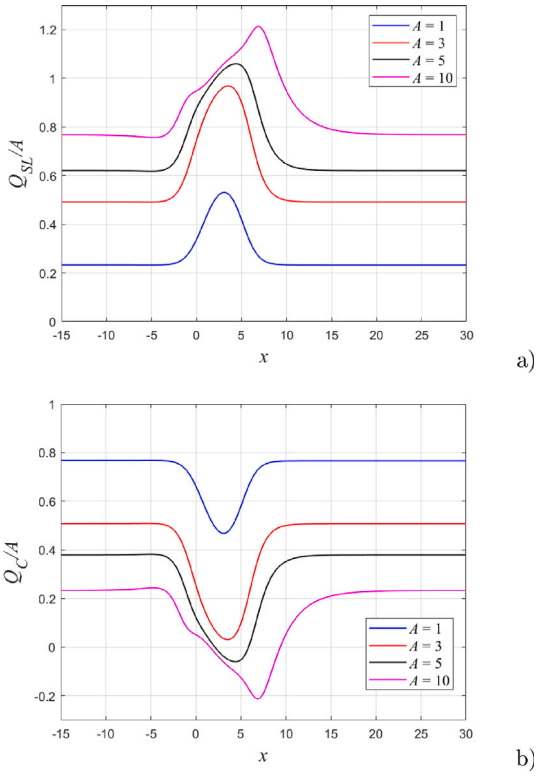

Fig. 25. Development of flow rate fractions carried by the Shercliff layer (a) and the core (b) for $c = 0.1$, $\gamma = 0.45$ and for several values of A. (AM).

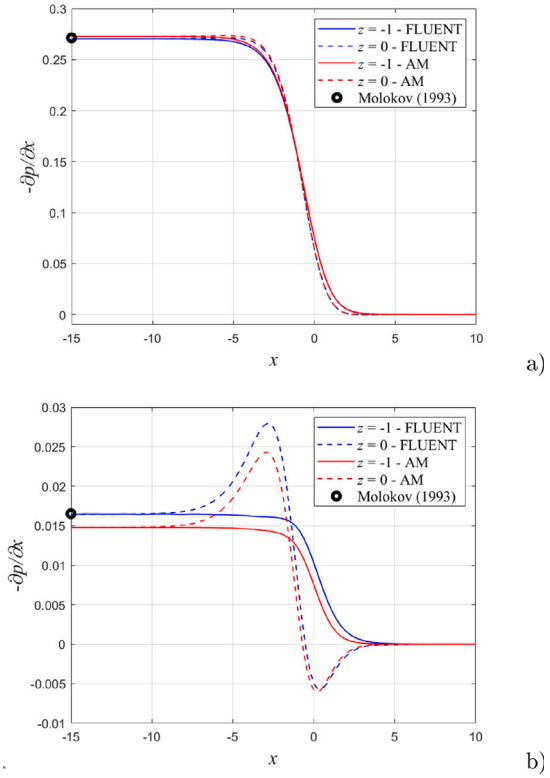

Fig. 26. Negative values of the longitudinal pressure gradient for a square duct at $y = 0$ and $z = -1$ (solid lines) and $z = 0$ (broken lines). Here $Ha = 5800$ and $c = 0.5$ (a) and $c = 0.02$ (b). The circles indicate corresponding pressure gradients in the fully developed flow calculated using the solution in [6].

References

[1] S. Smolentsev, Physical background, computations and practical issues of the magnetohydrodynamic pressure drop in a fusion liquid metal blanket, Fluids 6 (2021) 110, http://dx.doi.org/10.3390/fluids6030110.

[2] C. Mistrangelo, L. Bühler, C. Alberghi, S. Bassini, L. Candido, C. Courtessole, A. Tassone, F.R. Urgorri, O. Zikanov, MHD R & D activities for liquid metal blankets, Energies 14 (2021) 6640, http://dx.doi.org/10.3390/en14206640.

[3] T.R. Barrett, M. Bamford, N. Bowden, B. Chuilon, T. Deighan, P. Efthymiou, M. Gorley, T. Grant, D. Horsley, M. Kovari, M. Tindall, CHIMERA fusion technology facility: testing and virtual qualification, Fusion Sci. Technol. 79 (2023) 1039–1050, http://dx.doi.org/10.1080/15361055.2022.2147766.

[4] D.J. Temperley, L. Todd, The effects of wall conductivity in magnetohydrodynamic duct flow at high hartmann numbers, Math. Proc. Cambridge Philos. Soc. 69 (1971) 337–351, http://dx.doi.org/10.1017/S0305004100046752.

[5] J.S. Walker, Magnetohydrodynamic flows in rectangular ducts with thin conducting walls, J. de Mécanique 20 (1981) 79–112.

[6] S. Molokov, Fully developed liquid-metal flow in multiple rectangular ducts in a strong uniform magnetic field, Eur. J. Mech. B Fluids 12 (1993) 769–787.

[7] Th. Arlt, L. Bühler, Numerical simulations of time-dependent Hunt flows with finite wall conductivity, Magnetohydrodynamics 55 (2019) 319–336, http://dx.doi.org/10.22364/mhd.55.3.5.

[8] D. Krasnov, A. Akhtari, O. Zikanov, J. Schumacher, Tensor-product-Thomas elliptic solver for liquid-metal magnetohydrodynamics, J. Comput. Phys. 474 (2) (2023) 111784, http://dx.doi.org/10.1016/j.jcp.2022.111784.

[9] C.B. Reed, B.F. Picologlou, Sidewall flow instabilities in liquid metal MHD flow under blanket relevant conditions, Fusion Technol. 15 (1989) 705–715, http://dx.doi.org/10.13182/FST89-A39780.

[10] U. Burr, L. Barleon, U. Müller, A. Tsinober, Turbulent transport of momentum and heat in magnetohydrodynamic rectangular duct flow with strong sidewall jets, J. Fluid Mech. 406 (2000) 247–279, http://dx.doi.org/10.1017/S0022112099007405.

[11] Zengyu Xu, Chuanjie Pan, Wenhao Wei, Xiaoqiong Chen, Yanxu Zhang, Wenzhong Li, Experimental investigation and theoretical analysis of two-dimensional magnetohydrodynamic effects in a rectangular duct, Fusion Technol. 36 (1999) 47–51, http://dx.doi.org/10.13182/FST99-A90.

[12] J.C.R. Hunt, Magnetohydrodynamic flow in rectangular ducts, J. Fluid Mech. 21 (1965) 577–590, http://dx.doi.org/10.1017/S0022112065000344.

[13] T.Q. Hua, J.S. Walker, B.F. Picologlou, C.B. Reed, Three-dimensional magnetohydrodynamic flows in rectangular ducts of liquid-metal-cooled blankets, Fusion Technol. 14 (1989) 1389.

[14] C.B. Reed, B.F. Picologlou, T.Q. Hua, J.S. Walker, ALEX results – a comparison of measurements from a round and a rectangular duct with 3-D code predictions, in: 12th Symposium on Fusion Engineering, Monterey, California, October 13–16, IEEE, 1987, p. 1267.

[15] U. Müller, L. Bühler, Magnetofluiddynamics in Channels and Containers, Springer, Dordrecht, 2001.

[16] S. Molokov, G. Politis, Parametric study of liquid metal flows in conducting circular ducts in a strong nonuniform magnetic field, Fusion Eng. Des. 209 (2024) 114688, http://dx.doi.org/10.1016/j.fusengdes.2024.114688.

[17] S. Molokov, L. Bühler, Liquid metal flow in a U-bend in a strong uniform magnetic field, J. Fluid Mech. 267 (1994) 325–352, http://dx.doi.org/10.1017/S0022112094001205.

[18] S. Molokov, R. Stieglitz, Liquid-metal flow in a system of electrically coupled U-bends in a strong uniform magnetic field, J. Fluid Mech. 299 (1995) 73–95, http://dx.doi.org/10.1017/S0022112095003429.

[19] S. Aleksandrova, S. Molokov, Three-dimensional buoyant convection in a rectangular cavity with differentially heated walls in a strong magnetic field, Fluid Dyn. Res. 35 (2004) 37–66, http://dx.doi.org/10.1016/j.fluiddyn.2004.04.002.

[20] L. Bühler, Laminar buoyant magnetohydrodynamic flow in vertical rectangular ducts, Phys. Fluids 10 (1998) 223–236, http://dx.doi.org/10.1063/1.869562.

[21] K. Miyazaki, S. Inoue, N. Yamaoka, T. Horiba, K. Yokomizo, Magneto-hydrodynamic pressure drop of lithium flow in rectangular ducts, Fusion Technol. 10 (1986) 830–836, http://dx.doi.org/10.13182/FST10-830.

[22] J.S. Walker, Liquid-metal flow in a thin conducting pipe near the end of a region of uniform magnetic field, J. Fluid Mech. 167 (1986) 199–217, http://dx.doi.org/10.1017/S0022112086002793.

[23] M.-J. Ni, R. Munipalli, N.B. Morley, P. Huang, M.A. Abdou, A current density conservative scheme for incompressible MHD flows at a low magnetic Reynolds number. Part I: On a rectangular collocated grid system, J. Comp. Phy. 227 (2007) 174–204, http://dx.doi.org/10.1016/j.jcp.2007.07.025.

[24] X. Albets-Chico, E.V. Votyakov, H. Radhakrishnan, S. Kassinos, Effects of the consistency of the fringing magnetic field on direct numerical simulations of liquid–metal flow, Fusion Eng. Des. 86 (2011) 5–14, http://dx.doi.org/10.1016/j.fusengdes.2010.07.014.

[25] V. Klüber, L. Bühler, C. Mistrangelo, Numerical simulation of 3D magnetohydrodynamic liquid metal flow in a spatially varying solenoidal magnetic field, Fusion Eng. Des. 156 (2020) 111659, http://dx.doi.org/10.1016/j.fusengdes.2020.111659.

[26] Y. Jiang, S. Smolentsev, Characterization of the MHD flow and pressure drop in the access ducts of a liquid metal fusion blanket, Fusion Eng. Des. 201 (2024) 114262, http://dx.doi.org/10.1016/j.fusengdes.2024.114262.

[27] D. Suarez, A. Khodak, E. Mas de les Valls, L. Batet, A formal verification and validation of a low magnetic Reynolds number MHD code for fusion applications, IEEE Trans. Plasma Sci. 50 (2022) 4206–4212, http://dx.doi.org/10.1109/TPS.2022.3203801.

[28] A. Ting, J.S. Walker, T.J. Moon, C.B. Reed, B.F. Picologlou, Linear stability analysis for high-velocity boundary layers in liquid-metal magnetohydrodynamic flows, Internat. J. Engrg. Sci. 29 (1991) 939–948.

[29] J. Priede, S. Aleksandrova, S. Molokov, Linear stability of Hunt's flow, J. Fluid Mech. 649 (2009) 115–134, http://dx.doi.org/10.1017/S0022112009993259.

[30] T. Arlt, J. Priede, L. Bühler, The effect of finite-conductivity hartmann walls on the linear stability of Hunt's flow, J. Fluid Mech. 822 (2017) 880–891, http://dx.doi.org/10.1017/jfm.2017.322.

[31] M. Kinet, B. Knaepen, S. Molokov, Instabilities and transition in magnetohydrodynamic flows in ducts with electrically conducting walls, Phys. Rev. Lett. 103 (2009) 154501, http://dx.doi.org/10.1103/PhysRevLett.103.154501.

[32] L. Braiden, D. Krasnov, S. Molokov, T. Boeck, L. Bühler, Transition to turbulence in Hunt's flow in a moderate magnetic field, Europhys. Lett. 115 (2016) 44002, http://dx.doi.org/10.1209/0295-5075/115/44002.